Renewable Energy 237 (2024) 121544

Contents lists available at ScienceDirect

Renewable Energy

journal homepage: www.elsevier.com/locate/renene

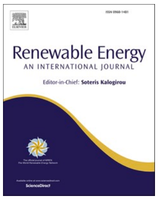

# Multi-objective spectral range optimization for different heat source temperatures to maximize thermophotovoltaic performance using NSGA-II

Xiu-Li Liu [a,b], Xiao-Lei Li [a,b], Xin-Lin Xia [a,b,*], Xue Chen [a,b]

[a] School of Energy Science and Engineering, Harbin Institute of Technology, Harbin, 150001, China
[b] Key Laboratory of Aerospace Thermophysics, Ministry of Industry and Information Technology, Harbin, 150001, China

ARTICLE INFO

*Keywords:*
Thermophotovoltaic
Internal quantum efficiency
Optimal spectral range
Non-dominated sorting genetic algorithm
Energy conversion

ABSTRACT

The energy conversion efficiency (ECE) and output power density of thermophotovoltaic (TPV) cells are mutually constraining. To better utilize this relationship, a framework was proposed to integrate the internal quantum efficiency (IQE) of TPV cells with a multi-objective genetic algorithm (NSGA-II) to optimize both efficiency and power density across diverse operating conditions. A spectrally selective emitter with a temperature of 1000–3000 K was selected as the radiation source for the studied TPV devices, capable of emitting a spectrum between 0.4 and 2.0 μm. The gallium antimonide (GaSb) cell was selected as the exploration cell, operating within a temperature range of 0–200 °C. Through theoretical calculation, the changes in physical parameters and *IQE* curves of GaSb cells at various temperatures were determined. The optimal spectral range for varying cell and emitter temperatures was determined using the NSGA-II algorithm. It was found that the *IQE* curve decreases with increasing temperature. Due to the spectral mismatch, the TPV conversion efficiency is much less than 20 % when the spectral range of the cell is 0.4–2.0 μm at room temperature. By incorporating *IQE* into the multi-objective optimization, the efficiency and power density distribution curves can be divided into three regions. In practical applications, the corresponding regions can be selected based on different efficiency and output power requirements.

Nomenclature

| *Latin symbols* | | | |
|---|---|---|---|
| | | $L_h$ | the minority holes diffusion length (m) |
| $c$ | speed of light in a vacuum ($3 \times 10^8$ m s$^{-1}$) | $T_0$ | reference temperature (300 K) |
| $D_h$ | drift velocity of the hole (m$^2$·s$^{-1}$) | $T_h$ | heat source (K) |
| $e$ | electron charge ($1.602 \times 10^{-19}$ C) | $T_e$ | spectral control emitter (K) |
| $E_E$ | the built-in electrostatic field | $T_c$ | cell temperature (K) |
| $E_g$ | band gap (eV) | $V_{oc}$ | open circuit voltage (V) |
| $G$ | carrier generation rate (m$^{-3}$·s) | *Greek Symbols* | |
| $h$ | Planck constant ($6.63 \times 10^{-34}$ J s) | $\eta$ | efficiency (%) |
| $h_a$ | Planck constant (W·m$^{-2}$·K$^{-1}$) | $\kappa$ | extinction coefficient |
| $k$ | Boltzmann constant ($1.38 \times 10^{-23}$ J s) | $\lambda$ | wavelength (μm) |
| $J_0$ | the reverse saturation current density (A/m$^2$) | $\tau$ | carrier lifetime (s) |
| $J_{sc}$ | the short-circuit current density (A/m$^2$) | $\alpha$ | absorption coefficient (m$^{-1}$) |
| $F$ | the view factor | *Abbreviations* | |
| $\mu_e$ | the electron mobility [cm$^2$(Vs)$^{-1}$] | *IQE* | Internal quantum efficiency (%) |
| $\mu_h$ | the electron mobility [cm$^2$(Vs)$^{-1}$] | TPV | thermophotovoltaic |
| $P_m$ | the maximum output power (W) | | |
| $n_i$ | intrinsic carrier concentration (m$^{-3}$) | | |

(*continued on next column*)

(*continued*)

## 1. Introduction

Thermophotovoltaic (TPV) is a promising energy conversion method that converts radiative energy into electrical energy [1]. A complete TPV system primarily consists of a heat source, an emitter, a filter, and a TPV cell [2]. The power generation principles of solar photovoltaic (PV) systems are similar to those of thermophotovoltaic (TPV) systems. The main difference lies in the source of energy: while the energy for solar PV systems is directly derived from the sun, the energy for TPV systems can be obtained from various sources, such as solar energy [3], combustion [4], nuclear energy [5], and waste heat sources [6], among others.

---

* Corresponding author. School of Energy Science and Engineering, Harbin Institute of Technology, Harbin, 150001, China
*E-mail address:* xiaxl@hit.edu.cn (X.-L. Xia).

https://doi.org/10.1016/j.renene.2024.121544
Received 28 May 2024; Received in revised form 29 September 2024; Accepted 5 October 2024

Moreover, TPV systems offer several advantages over solar PV, such as high energy density, low noise and pollution, independence from time and space constraints, as well as enhanced safety and reliability [7]. Therefore, TPV power generation has great potential for applications, especially in cogeneration [8] and waste heat recovery [9]. However, according to the current research, the low energy conversion efficiency (ECE) of the TPV system is the main factor restricting its further development. The ECE of the system is affected by many factors, among which the most important is heat loss due to the spectral matching between the cell and emitter.

In earlier research, most research focused on improving the efficiency of the whole TPV system. A TPV system utilizing bioenergy as the heat source was designed by Erik et al. [10].

The cell and emitter were placed at the end of the vertebral structure, and a filter was placed at the middle midsection. During the experiment, the emitter was heated to 1200 °C, and the GaSb cell achieved an output power of 7.5 W, with an ECE reaching 4 %. Chan et al. [11] proposed a micro-thermophotovoltaic (μTPV) generator to produce power with high energy density, high efficiency, and portability. The μTPV is composed of a silicon propane micro-combustor, a selective thermal emitter, four indium gallium antimonide arsenide (InGaAsSb) cells, and a power-point tracking power electronics converter. It was shown that when the temperature of the mic-combustor reached 800 °C, an output power of 13.7 W was achieved, corresponding to a power density of 344 mW/cm$^2$. An ECE of 2.5 % t was achieved in the system during experimental tests. A gas-fired furnace system was designed by Qiu and Hayden [12]. The heat radiation was provided via a metal alloy emitter and an InGaAsSb cell with a band gap of 0.53 eV. The results showed that when the emitter temperature is 1197 °C, the output electric power density is 0.65 W/m$^2$. An electrical efficiency of 4.7 % is achieved in this TPV system. Li and Xuan [13] designed a hybrid thermophotovoltaic-thermoelectric system. The system consists of the gallium antimonide (GaSb) TPV cell and a $Bi_2Te_3$ thermal electric module. These two modules are installed without physical contact, thereby eliminating thermal interaction. The experimental results demonstrated that the efficiency of the TPV system could be enhanced, reaching a total efficiency of 5.91 %. López et al. [14] presented an experimental setup, and high TPV conversion efficiency is achieved by reducing the distance(<1 mm) from the emitter to the cell. Consequently, when the temperature of a graphite thermal emitter is 1592 °C, an output power density of 4.3 ± 0.8 W/cm$^2$ and a TPV efficiency of 26.4 ± 0.1 % were achieved by the indium gallium antimonide (InGaAs) cell with a back reflector. The above studies are aimed at enhancing the functionality of the complete TPV system. According to these experimental results, power density and conversion efficiency can be improved. However, the high cost remains a significant barrier to widespread application.

Some researchers focused on improving individual components in the TPV system. Meng et al. [15] designed a selective emitter with a core-shell nanosphere (CSN) structure. The emissivity of the emitter is as high as 0.93 within the effective bandgap by adjusting its geometric parameters. For a TPV system with InGaAs cells, an output power density of 0.594 W/cm$^2$ and the system efficiency of 12.83 % were achieved at an emitter temperature of 1338 K. Omair et al. [16] proposed that a rear mirror could be placed at the back of the cell. This mirror can recycle infrared thermal photons by reflecting low-energy infrared photons back to the heat source. By adding this reflective rear mirror design, the TPV efficiency of 29.1 ± 0.4 % was achieved at an emitter temperature of 1207 °C. Gamel et al. [17] suggested that TPV cells should be optimized to increase power output. To achieve multi-dimensional optimization of $In_{0.53}Ga_{0.47}As$, a precisely coded genetic algorithm was employed. The results showed that an output power of 0.55 W/cm$^2$ and a cell efficiency of 22.06 % can be achieved by the optimized TPV cell under the 1400 K emitter spectrum. According to the above research, the ultimate goal of optimizing individual components in the TPV system is to achieve spectral matching between the emitter and the TPV cell.

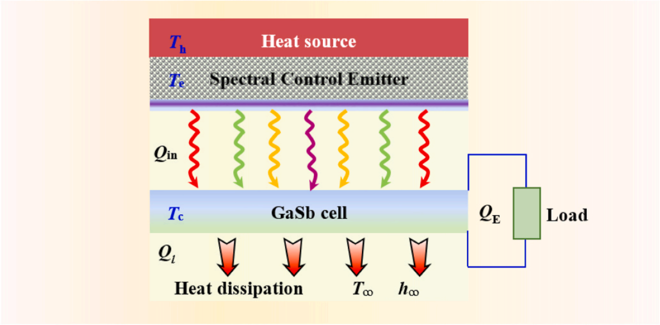

**Fig. 1.** Schematic of a typical thermophotovoltaic system.

In fact, the primary cause of low TPV conversion efficiency is the various heat losses associated with the cell. The heat loss mainly comes from Joule heating, thermalization of radiation, non-radiative recombination, and so on. Significant efforts have been dedicated to mitigate the negative impacts of these losses in TPV devices [18,19]. Many papers have been conducted to optimize the spectral matching between the emitter and the cell to minimize heat loss. However, it is crucial to note that an increase in cell temperature can further impact spectral matching between the emitter and the cell, thereby exacerbating heat loss. To the best of our knowledge, no attempt has been made to incorporate the quantum efficiency of the cell to achieve the maximum conversion efficiency when determining the optimal spectral range.

The objective of this work is to determine the optimal spectral range of TPV cells at different temperatures corresponding to different emitter temperatures, to maximize TPV cell utilization, and to rationalize efficiency and power density in different working environments. This is achieved by using a rigorous optimization framework that integrates an internal quantum efficiency model with a publicly available multi-objective genetic algorithm (NSGA-II). A spectrally selective radiator and a GaSb cell were selected as the research subjects. The temperature range of the spectrally selective radiator is 1000–3000 K [20], and its corresponding spectral range is 0.4–2.0 μm. The temperature range of the GaSb cell is 0–200 °C [21–23]. Through the temperature-dependent formula, the *IQE* curve of the GaSb cell at different temperatures is obtained. Subsequently, the optimal spectral range of the cell at various temperatures and radiation temperatures was determined using the NSGA-II method.

## 2. Mathematical model

Given that the temperatures of the TPV cell and the emitter are interdependent, determining the optimal radiator emission spectrum that maximizes TPV performance (energy conversion efficiency $\eta$ and output power $P$) is not a straightforward task. In practical applications, the temperature of the TPV cell is greater than the ambient temperature, rather than being at an ideal working temperature. Even if temperature management is adopted, it is not easy to reach an appropriate temperature. Therefore, to optimize the spectral matching between the heat source and the TPV cell at various temperatures and maximize TPV cell performance, a coupled electric-thermal TPV cell model is developed and integrated with the NSGA-II method.

In this study, multi-objective optimization is accomplished using NSGA-II [24,25]. Compared to other optimization algorithms, such as Grey Wolf Optimizer (GWO) [26], butterfly optimization algorithm (BOA) [27], and Particle Swarm Optimization (PSO) [28], this method offers the advantages of a uniformly distributed Pareto-optimal front, time-consuming calculation, and presenting the Pareto-optimal solution in a single run only in NSGA-II [29].

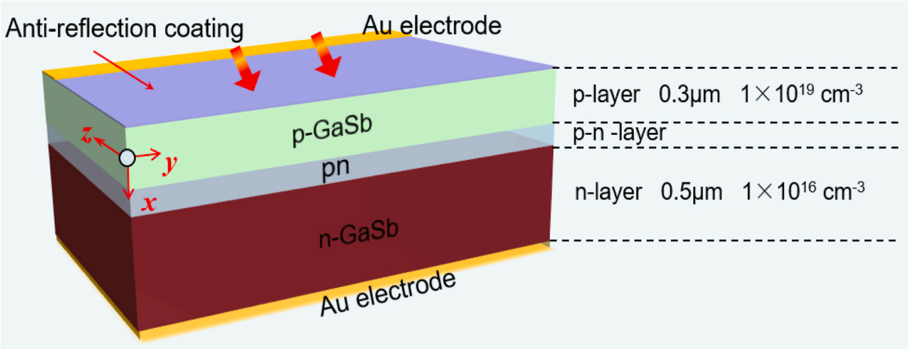

**Fig. 2.** The structure of GaSb Cell.

### 2.1. *Typical thermophotovoltaic system model*

Fig. 1 presents a schematic diagram of a typical TPV system. A heat source, selective emitter, TPV cell, and cooling system are included in the system. $T_h$, $T_e$, and $T_c$ denote the temperature of the heat source, the spectral control emitter, and the cell, respectively. In this study, it will be assumed that the $T_h$ and $T_e$ are equal. Meanwhile, considering the thickness of the cell is only 0.65 mm, the temperature difference between the top and bottom sides can be ignored. Based on the principle of energy conservation, the system energy equation is as follows:

$$\dot{Q}_{in} = \dot{Q}_e + \dot{Q}_l \tag{1}$$

where $\dot{Q}_{in}$ is the net radiation heat transfer between the emitter and cell, $\dot{Q}_e$ is the output power density of the GaSb cell, and $\dot{Q}_l$ is the heat loss of the heat dissipation system. According to the principle of conservation of energy, there is an inverse relationship between electrical energy and heat loss.

A vertical orientation of the emitter and the TPV cells $\dot{Q}_{in}$ can be calculated as follows [30]:

$$\dot{Q}_{in} = n^2 \varepsilon \sigma F A \left(T_e^4 - T_c^4\right) \tag{2}$$

where $n$ is the refractive index of the participating medium. $\varepsilon$ is the emissivity. $F$ is the view factor which is determined by the geometrical arrangement of system. $A$ is the active area of the cell.

The output power density is an important parameter that can be used to evaluate the performance of the TPV system. The calculation expression is as follows [31]:

$$\dot{Q}_e = J_{ph} V_{oc} \left[1 - \frac{1}{\ln(J_{ph}/J_0)}\right] \left[1 - \frac{\ln(J_{ph}/J_0)}{J_{ph}/J_0}\right] \tag{3}$$

where $J_{ph}$, $J_0$, and $V_{oc}$ are photocurrent density, reverse saturation current density, and open-circuit voltage, respectively.

The photocurrent density can be calculated by the internal quantum efficiency (*IQE*), and it can be expressed as follows [32]:

$$J_{ph} = \int_{\lambda_1}^{\lambda_2} \frac{e\lambda}{hc} \cdot IQE \cdot \alpha(\lambda) \dot{Q}_{in}(\lambda) d\lambda \tag{4}$$

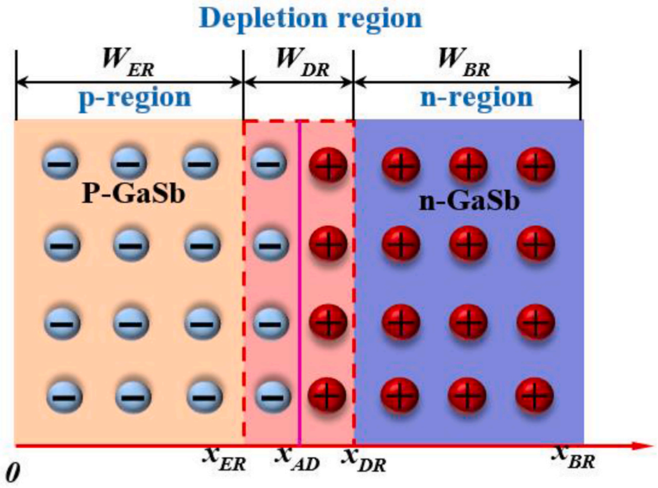

**Fig. 3.** The GaSb cell model and the width of each region.

where $\alpha(\lambda)$ is the absorption coefficient of the cell. $c$ represents the speed of light. $e$ represents the unit charge. $h$ represents the Planck constant. $\lambda_1$ and $\lambda_2$ are the boundary wavelengths of the selective spectrum. *IQE* is the total internal quantum efficiency that can be provided by manufacturers. However, the *IQE* curve of the cell provided by the producer only represents the spectral conversion performance of the cell at room temperature. In fact, the *IQE* curve varies with the cell temperature, thereby affecting the energy conversion performance of different bands. Meanwhile, the energy loss of the cell in the response band is extremely high, especially under a high-temperature heat source. Even if certain heat dissipation measures are taken, the temperature of the cell is still significant. The heat dissipation can be expressed as follows [33]:

$$\dot{Q}_l = h_a (T_c - T_\infty) \tag{5}$$

where $T_\infty$ is the temperature of the ambient. $h_a$ is the convective heat transfer coefficient, which is determined by different heat dissipation methods.

### 2.2. *The thermophotovoltaic cell-genetic algorithm model*

#### 2.2.1. *A model for calculating IQE curve of the TPV cell*

In this work, the structure of the GaSb cell is shown in Fig. 2. GaSb is a narrow band gap III-V semiconductor material, which is formed by the combination of p-type and n-type semiconductors to form a p-n junction [34,35]. It is not only easy to manufacture but has also been demonstrated as a promising candidate for high-speed electronic and infrared photonic devices such as lasers, detectors, and thermophotovoltaic cells [36]. Within the past few years, both the Fraunhofer Institute for Solar Energy System (FISE) and JX Crystals have been able to manufacture high-quality GaSb cells and sell them to the public. Therefore, the widely used GaSb cell was selected for this study. The operating principle of the GaSb cell is as follows: When photons are absorbed by semiconductor materials, minority carriers (electrons and holes) are generated in both the conduction and valence bands. Although there is a powerful built-in electric field in the barrier area of the p-n junction, with the increase of the concentration of minority carriers, they can enter the barrier area through diffusion. Due to the built-in electrostatic field, they move in opposite directions and leave the depletion region, causing the potential in the p region to increase and the potential in the n region to decrease, and ultimately establishing a potential difference across the p-n junction. When the external circuit is connected, the carriers flow through the circuit, generating a current.

To simplify the calculation model, the $x$-direction is expanded, and only three regions are considered [37]. The structure of these three regions is illustrated in Fig. 3. They are referred to as the emitter region (ER), the depletion region (DR), and the base region (BR). The ER is a p-type semiconductor with a width denoted as $W_{\mathrm{ER}}$. The DR is the pn junction of the GaSb cell, with a width of $W_{\mathrm{DR}}$. The BR is an n-type semiconductor with a width of $W_{\mathrm{BR}}$. The built-in electrostatic field in this region is oriented in the opposite direction to the potential difference outside the cell.

Before calculating the *IQE* of the GaSb cell, the spectral distribution of the emitter needs to be defined. In this work, a spectrally selective emitter is selected as the radiation source, with the spectral range is 0.4–2.0 μm. It is assumed that the emissivity of the spectrally selective emitter in the effective spectral range is comparable to that of a blackbody. According to Planck's law, the spectral distribution of blackbody radiation is given by the following equation:

$$E_{\mathrm{b}}(\lambda, T_{\mathrm{r}}) = \frac{2\pi hc^2}{\lambda^5\left[\exp\left(\frac{hc}{k\lambda T_{\mathrm{r}}}\right) - 1\right]} \tag{6}$$

where $k$ is the Boltzmann constant. $T_{\mathrm{r}}$ is the temperature of the blackbody heat source. $\lambda$ is the wavelength.

The intrinsic carrier concentration $n_{\mathrm{i}}$ is a crucial parameter for achieving precise calculations in TPV cells. To estimate the $n_{\mathrm{i}}$ value accurately, it is necessary to consider the energy gap of the semiconductor $E_{\mathrm{g}}$, the effective density of states in the valence band $N_{\mathrm{v}}$, and the effective density of states in the conduction band $N_{\mathrm{c}}$. It is given by the following expression [38]:

$$n_{\mathrm{i}} = \sqrt{N_{\mathrm{c}}N_{\mathrm{v}}}\exp\left(-\frac{E_{\mathrm{g}}}{2kT_{\mathrm{c}}}\right) \tag{7}$$

where $N_{\mathrm{c}}$ and $N_{\mathrm{v}}$ are the functions of temperature, $N_{\mathrm{c}} = 2\cdot(2\pi m_{\mathrm{n}}{*}kT)^{3/2}/h^3$ and $N_{\mathrm{v}} = 2\cdot(2\pi m_{\mathrm{p}}{*}k\mathrm{T})^{3/2}/h^3$. $m_{\mathrm{n}}*$ and $m_{\mathrm{p}}*$ represent the effective mass of electrons and holes, respectively. The formula can be further written as follows [39]:

$$n_i = 2\left(\frac{2\pi m_0 kT}{h^2}\right)^{\frac{3}{2}}\left(m_{\mathrm{e,L}}^{*\frac{3}{2}}\exp\left(\frac{-\Delta E_{\Gamma,\mathrm{L}}}{kT}\right) + m_{\mathrm{e},\Gamma}^{*\frac{3}{2}}\right)^{\frac{1}{2}} \times \left(m_{\mathrm{h},\psi}^{*\frac{3}{2}} + m_{\mathrm{h},\gamma}^{*\frac{3}{2}}\right)^{\frac{1}{2}}\exp\left(\frac{-E_{\mathrm{g}}}{2kT}\right) \tag{8}$$

where $m_{\mathrm{e,L}}^{*\frac{3}{2}}$ and $m_{\mathrm{e},\Gamma}^{*\frac{3}{2}}$ represent the $L$ layer and $\Gamma$ layer of the mass of electronic effects in the conduction band, respectively. $m_{\mathrm{h},\psi}^{*\frac{3}{2}}$ and $m_{\mathrm{h},\gamma}^{*\frac{3}{2}}$ represent the $\psi$ layer and $\gamma$ layer of the mass of the hole in the valence band, respectively. $m_0$ is the mass of the free electron, $m_0 = 9.1095 \times 10^{-31}$ kg.

The semi-empirical formula proposed by Varshini [40] is used to give the dependence of band gap energy with temperature:

$$E_{\mathrm{g}} = E_{\mathrm{g0}} - \frac{AT^2}{T+B} \tag{9}$$

where $E_{\mathrm{g0}}$ represents the band gap energy of the cell at 300 K. According to the empirical data in Frass [41] literature, taken $E_{\mathrm{g0}} = 0.812$ eV, $A = 4.17417 \times 10^{-4}$ eVK$^{-1}$, and $B = 140$ K, respectively.

There is an inverse relationship between the cutoff wavelength($\lambda_{\mathrm{c}}$) and the bandgap energy:

$$\lambda_{\mathrm{c}} = \frac{hc}{E_g} \tag{10}$$

The mobility of electrons and holes is calculated using Martin's [42] semi-empirical formula:

$$\mu_{\mathrm{e}}(N_{\mathrm{D}}, T) = \mu_{\mathrm{min,e}} + \frac{\mu_{\mathrm{max,e}}(300/T)^{\theta_{1,\mathrm{e}}} - \mu_{\mathrm{min,e}}}{1 + \left(N_{\mathrm{D}}\Big/N_{\mathrm{ref,e}}(300/T)^{\theta_{2,\mathrm{e}}}\right)^{\alpha_{\mathrm{e}}}} \tag{11}$$

where the maximum and the minimum electron mobility are $\mu_{\mathrm{max,e}} = 5650$ cm$^2$(Vs)$^{-1}$ and $\mu_{\mathrm{min,e}} = 1050$ cm$^2$(Vs)$^{-1}$, respectively. $N_{\mathrm{ref,e}}$ is the doping concentration at which the mobility is decreased to half the value it reaches at low doping, at room temperature, $N_{\mathrm{ref,e}} = 2.8 \times 10^{17}$ cm$^{-3}$. $\alpha_{\mathrm{e}}$ represent the absorption coefficient of electron, $\alpha_{\mathrm{e}} = 1.05$, $\theta_{1,\mathrm{e}}$ and $\theta_{2,\mathrm{e}}$ represent the temperature coefficient of electron, $\theta_{1,\mathrm{e}} = 2.0$, $\theta_{2,\mathrm{e}} = 2.8$.

Similar to the electron mobility, the hole mobility is expressed as follows [42]:

$$\mu_{\mathrm{h}}(N_{\mathrm{A}}, T) = \mu_{\mathrm{min,h}} + \frac{\mu_{\mathrm{max,h}}(300/T)^{\theta_{1,\mathrm{e}}} - \mu_{\mathrm{min,h}}}{1 + \left(N_{\mathrm{D}}\Big/N_{\mathrm{ref,h}}(300/T)^{\theta_{2,\mathrm{h}}}\right)^{\alpha_{\mathrm{h}}}} \tag{12}$$

where $\mu_{\mathrm{max,h}} = 875$ cm$^2$(Vs)$^{-1}$, $\mu_{\mathrm{min,h}} = 190$ cm$^2$(Vs)$^{-1}$, $N_{\mathrm{ref,h}} = 9 \times 10^{17}$ cm$^{-3}$, $\alpha_{\mathrm{e}} = 0.65$, $\theta_{1,\mathrm{e}} = 1.7$, $\theta_{2,\mathrm{e}} = 2.7$.

The generation rate of minority carriers is the function of the input spectral irradiance and semiconductor absorption coefficient $\alpha(\lambda)$, it can be calculated as follows [43]:

$$G(x, \lambda) = \dot{Q}_{\mathrm{in}}(\lambda)\alpha(\lambda)\exp[-\alpha(\lambda)x] \tag{13}$$

where the $x$ represents the direction along the thickness of the cell.

The total quantum efficiency of the cell consists of three parts: the ER region $QE_{\mathrm{ER}}(\lambda)$, the DR region, $QE_{\mathrm{DR}}(\lambda)$, and the BR region, $QE_{\mathrm{BR}}(\lambda)$. Therefore, the total internal quantum efficiency of the GaSb cell is expressed as follows [44]:

$$IQE(\lambda) = QE_{\mathrm{ER}}(\lambda) + QE_{\mathrm{DR}}(\lambda) + QE_{\mathrm{BR}}(\lambda) \tag{14}$$

$QE_{\mathrm{ER}}(\lambda)$ can be calculated by the current density of the minority carrier [45]:

$$QE_{\mathrm{ER}}(\lambda) = \frac{J_e(x, \lambda)|_{x=x_{\mathrm{ER}}}}{e\dot{Q}_{\mathrm{in}}(\lambda)} = \frac{[en(x)\mu_{\mathrm{e}}(x)E_{\mathrm{E}}(x) + kT\mu_{\mathrm{e}}(x)(dn(x)/dx)]|_{x=x_{\mathrm{ER}}}}{e\dot{Q}_{\mathrm{in}}(\lambda)} \tag{15}$$

where $J_{\mathrm{e}}$ $(x, \lambda)$ is the density of minority carriers at the emitter edge $x = x_{\mathrm{ER}}$. $E_{\mathrm{E}}$ represents the built-in electrostatic field.

$QE_{\mathrm{DR}}(\lambda)$ can be calculated as follows [46]:

$$QE_{\mathrm{DR}}(\lambda) = \alpha(\lambda)\exp[-\alpha(\lambda)W_{\mathrm{ER}}](1 - \exp[-\alpha(\lambda)W_{\mathrm{DR}}]) \tag{16}$$

where the $W_{\mathrm{ER}}$ and $W_{\mathrm{DR}}$ represent the width of the ER and DR, respectively.

Given the constant doping concentration of the donor and the width of the BR ($W_{\mathrm{BR}}$), the $QE_{\mathrm{BR}}$ can be calculated by Bouzid's formula [47]:

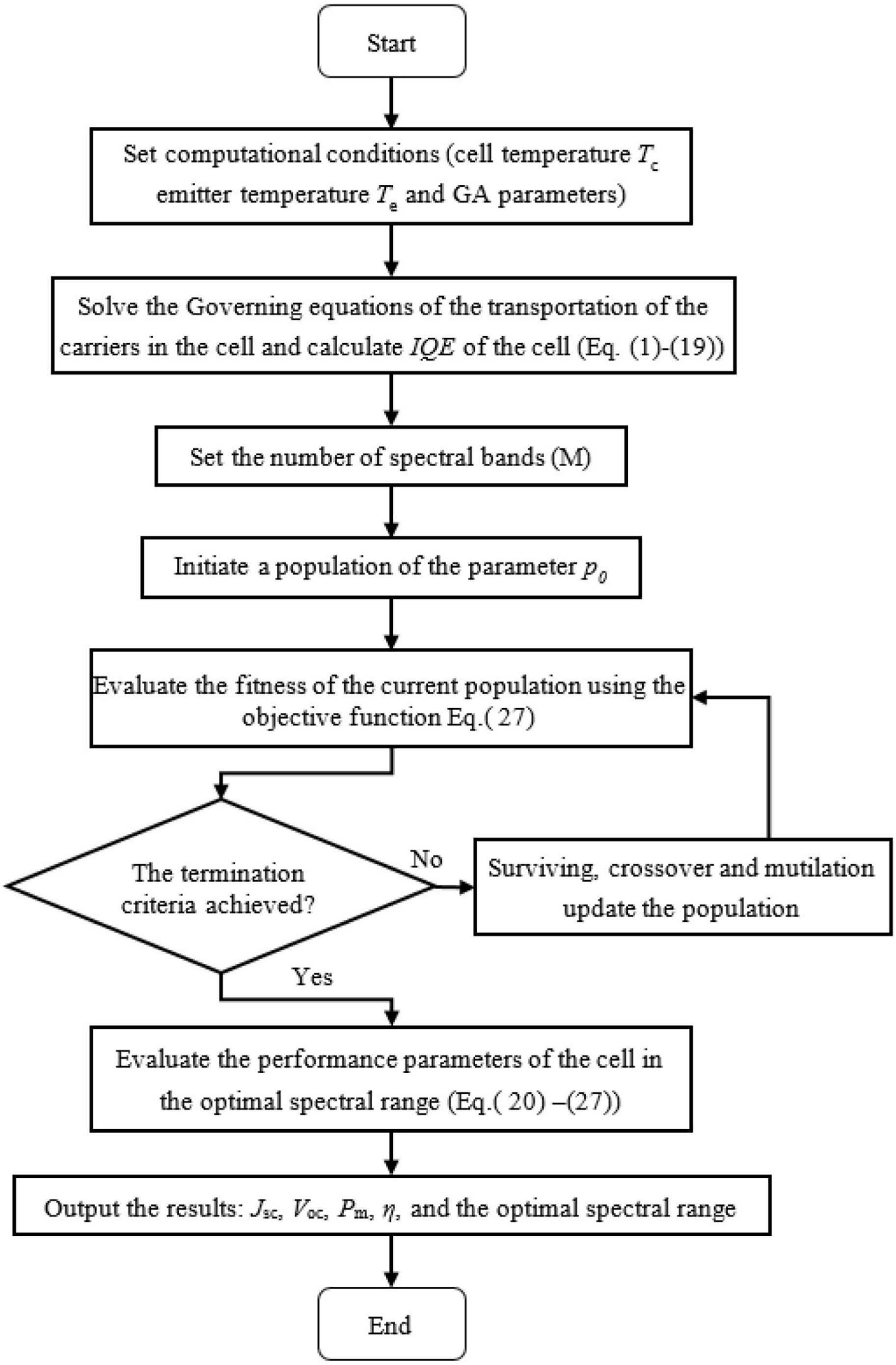

**Fig. 4.** Flowchart of genetic algorithm method to find the best matching range between different spectral radiation and the TPV cell.

$$\mathrm{QE}_{\mathrm{BR}}(\lambda) = \frac{\alpha(\lambda)L_{\mathrm{h}}}{1+\alpha(\lambda)L_{\mathrm{h}}}\exp[-\alpha(\lambda)(W_{\mathrm{ER}}+W_{\mathrm{DR}})] \tag{17}$$

where the $L_{\mathrm{h}}$ represents the diffusion length of the minority carrier (holes), it is calculated as follows [48]:

$$L_{\mathrm{h}} = \sqrt{D_{\mathrm{h}}\tau_{\mathrm{h}}} \tag{18}$$

where the $\tau_{\mathrm{h}}$ represents the lifetime of the hole. The $D_{\mathrm{h}}$ represents the drift velocity of the hole. According to Einstein's equation, it is represented as follows [49]:

$$D_{\mathrm{h}} = (kT/e)\mu_{\mathrm{h}} \tag{19}$$

The reverse saturation current of the cell is calculated as follows [50]:

$$J_0 = eN_cN_v[D_{\mathrm{n}}/(L_{\mathrm{n}}N_{\mathrm{A}}) + D_{\mathrm{p}}/(L_{\mathrm{p}}N_{\mathrm{D}})]\exp[-E_g/kT] \tag{20}$$

By bringing the $N_c$ and $N_v$ into equation (13), the reverse saturation current, temperature, and the band gap have the following relationships [23]:

$$J_0 = CT^3\exp\left(\frac{-E_g(T)}{kT}\right) \tag{21}$$

where $C$ is an empirical constant taken as 1.84 × 10-3 $\mathrm{Am}^{-2}\mathrm{K}^3$ [41].

The short-circuit current ($J_{sc}$) is calculated as follows [51]:

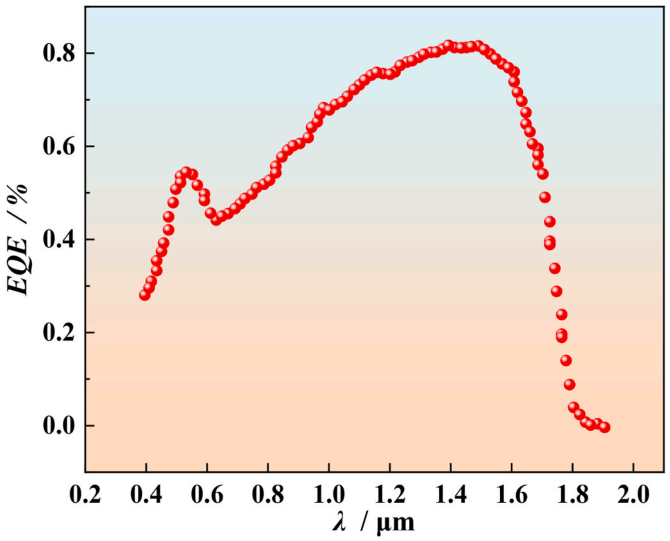

**Fig. 5.** The *EQE* of GaSb cell at room temperature.

$$J_{sc} = eN_{ph} = eF\int_{\lambda_1}^{\lambda_2} \frac{E(b,\lambda)\cdot\alpha(\lambda)\cdot IQE(\lambda)d\lambda}{hc/\lambda} \tag{22}$$

where $F$ is taken as 1.

The open-circuit voltage ($V_{oc}$) can be calculated as follows [52]:

$$V_{oc} = (kT/e)\ln[J_{sc}/J_0 + 1] \tag{23}$$

The transcendental equation can be used to solve the maximum voltage [53]:

$$V_{oc} = (kT/e)\ln\left[1 + eV_{mp}/kT\right] + V_{mp} \tag{24}$$

where the $V_{mp}$ represents the maximum voltage point.

The maximum power ($P_m$) is calculated as follows [54]:

$$P_m = eJ_{sc}\left(V_{mp}\right)^2 / \left(kT_c + eV_{mp}\right) \tag{25}$$

The conversion efficiency of the cell is calculated as follows [55]:

$$\eta = \frac{P_m}{\dot{Q}_{in}} \tag{26}$$

The fitness function is defined as $f(\lambda)$, and it is shown in Eq. (27):

$$\text{Minmimize}: \begin{cases} f_1(\lambda_1,\lambda_2) = \dfrac{\displaystyle\int_{\lambda_1}^{\lambda_2}(1 - IQE_\lambda)E_{b,\lambda}d\lambda}{\displaystyle\int_{\lambda_1}^{\lambda_2}E_{b,\lambda}d\lambda} \\ f_2(\lambda_1,\lambda_2) = \dfrac{1}{P_m} \end{cases} \tag{27}$$

Subject to: 0.4 μm< $\lambda_1 < \lambda_2 < 2.0$ μm.

where $E_{b,\lambda}$ characterizes the relationship between spectral energy distribution and temperature, and the *IQE* characterizes the relationship between heat source temperature and cell temperature.

### 2.2.2. Coupling of the IQE model with the NSGA-II

According to Eqs. (6)–(19), the *IQE* can be calculated. To explore the best matching range between different spectral emitters and TPV cells in various working environments and to identify the emitter emission spectrum that maximizes TPV performance, the NSGA-II method, a highly efficient optimization tool, is coupled with the TPV cell model to obtain the optimal spectral range under different operating conditions.

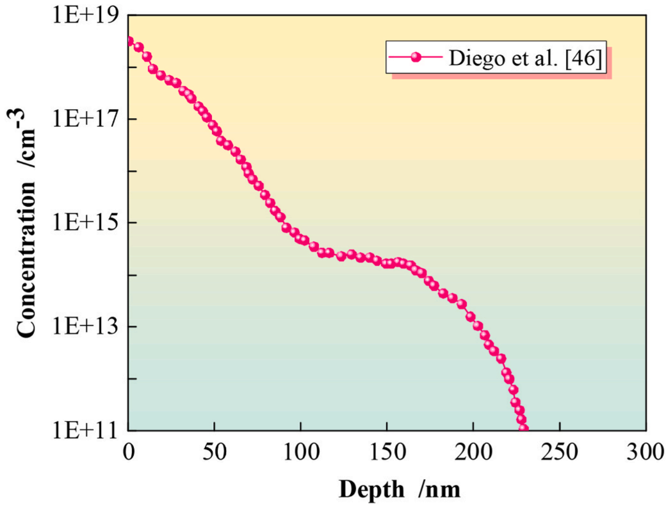

**Fig. 6.** Diffusion concentration distribution of GaSb cell.

Considering the spectral response range of the GaSb cell, the spectral range of the spectrally selective emitter is set to 0.4–2.0 μm. The emission spectrum is discretized into M small intervals within this range (0.4–2.0 μm), with a spectral emissivity of 1 for each interval. The NSGA-II method is used to find a group of optimal individuals in this range, maximize the fitness function, and achieve the maximum TPV conversion performance. A random population of emission spectra at any temperature is generated to initialize the NSGA-II calculation. In each discretized spectral range, $P_m$ is calculated using the *IQE* model. Based on the $P_m$ values obtained for each band, a ranking is established. The *IQE*-NSGA-II -GA algorithm schematic for determining the $\eta$ is illustrated in Fig. 4.

In this work, the temperature range of the spectrally selective emitter ($T_e$)is set to 1000–3000 K, and the temperature range of the cell ($T_c$) is 0–200 °C. The $W_{ER} = 0.03$ μm, while $W_{BR} = 0.5$ μm. It is assumed that the thickness of the depletion region is confined to the p-type region, which varies with the temperature. Since the temperature difference between the two sides of the cell is less than 0.1 K, it is considered negligible. In this work, the cell temperature refers to the average temperature of the cell. A population size of 100 with an evolutionary period of 2000 generations proved to be sufficient for determining the emission spectra that maximize $\eta$ or $P$ in all simulation calculations. Refinement of temperature discretization did not significantly alter the emission spectrum. This suggests that the current configuration is optimal for maximizing the conversion efficiency of the cell. The stability and reliability of the results are thus ensured.

## 3. Results and discussion

### 3.1. Cooling system heat dissipation

As provided by manufacturers, the external quantum efficiency (*EQE*) of the GaSb cell at room temperature is shown in Fig. 5. It can be inferred from the graph that the GaSb cell can operate effectively in the spectral range of 0.4–2.0 μm, while energy outside this range cannot be utilized. Unusable energy can be converted into heat, causing the temperature of the cell to rise and posing a greater burden on heat dissipation. Assuming the temperature of the blackbody heat source is 1000 K, the energy within the operating band of the cell is about 0.56 W, while the energy outside this band is around 7.83 W. The latter is approximately 14 times greater than the former. This unutilized energy will result in significant waste heat generation.

According to existing literature, various cooling methods are available, but the convective heat transfer coefficient is relatively low. For example, when the cell is immersed in circulating water with forced

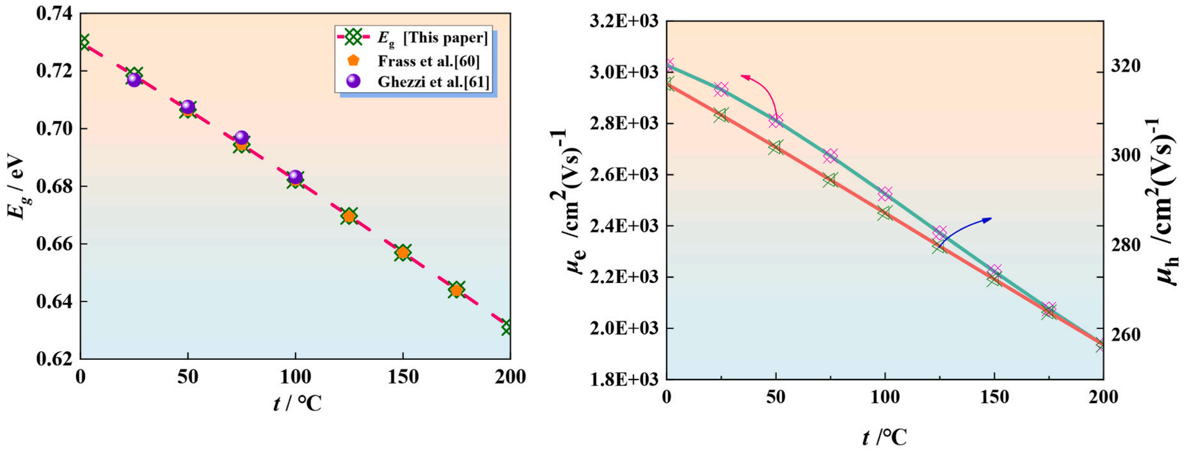

(a) the bandgap energy

(b) the mobility of electrons and hole

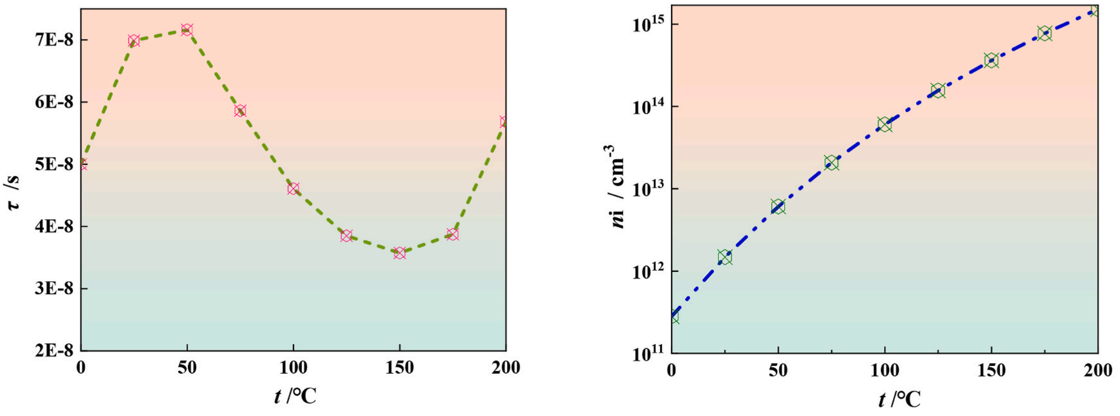

(c) the carrier lifetime

(d) the intrinsic carrier concentration

**Fig. 7.** Effect of cell temperature on cell performance parameters.

convection for heat dissipation, a convective heat transfer coefficient of $6 \times 10^3$ W/(m$^2$·K) can be achieved [56]. If high-pressure water is used to directly impinge the photovoltaic cell, the coefficient can be increased to $2.7 \times 10^4$ W/(m$^2$·K) [57]. For a single channel system, the required convective heat transfer must reach $3.5 \times 10^4$ W/(m$^2$·K) to effectively cool the TPV cell [58]. When using a multi-channel flow configuration, the maximum convection heat transfer coefficient needs to be as high as $6.5 \times 10^4$ W/(m$^2$·K) [59]. Achieving these values is essential to maintain the cell at ambient temperature.

As mentioned above, for high-temperature emitters, the cell requires highly efficient heat dissipation, making it extremely challenging to maintain a constant temperature of 300 K. However, once the temperature of the cell changes, the internal quantum efficiency curve of the cell will be changed. Therefore, to improve the working performance of the cell under a high-temperature emitter, the optimal spectral range of the cell at different heat sources and cell temperatures is selected as needed.

### 3.2. The change in the physical parameters

According to the calculation model of *IQE*, the energy conversion efficiency of the cell is significantly affected by the doping concentration of the donor and acceptor. Therefore, in this study, we assume a non-uniform doping [46], as illustrated in Fig. 6, which shows the concentration distribution across the cell.

According to the above calculation model of *IQE*, the influence of temperature on various parameters can be observed, as shown in Fig. 7. The bandgap energy and carrier mobility of the cell are both negatively correlated with temperature (Fig. 7 (a)(b)), decreasing as the cell temperature increases. Meanwhile, the results of the bandgap energy variation with temperature were compared with those in Frass et al. [60] and Ghezzi et al. [61], showing good agreement, which suggests that our findings are reasonably accurate. The carrier lifetime (Fig. 7 (c)) exhibits an S-shaped variation with temperature, increasing in the ranges of 0–50 °C and 150–200 °C as the temperature rises. The intrinsic carrier concentration (Fig. 7 (d)) is positively correlated with temperature, gradually increasing as the temperature rises. The reason behind this phenomenon is that as the temperature increases, the energy of the carrier also rises, enabling it to surpass the energy band gap and transition into the energy band, leading to a surge in carrier concentration.

### 3.3. The IQE curves at different temperatures

According to the curve movement in Fig. 8, the temperature has a significant influence on the *IQE* of different regions (ER, DR, and BR). In Fig. 8 (a), the peak value of ER conversion efficiency is about 40 %. As the cell temperature increases, the peak value of conversion efficiency experiences a redshift. Beyond the peak, as the wavelength increases,

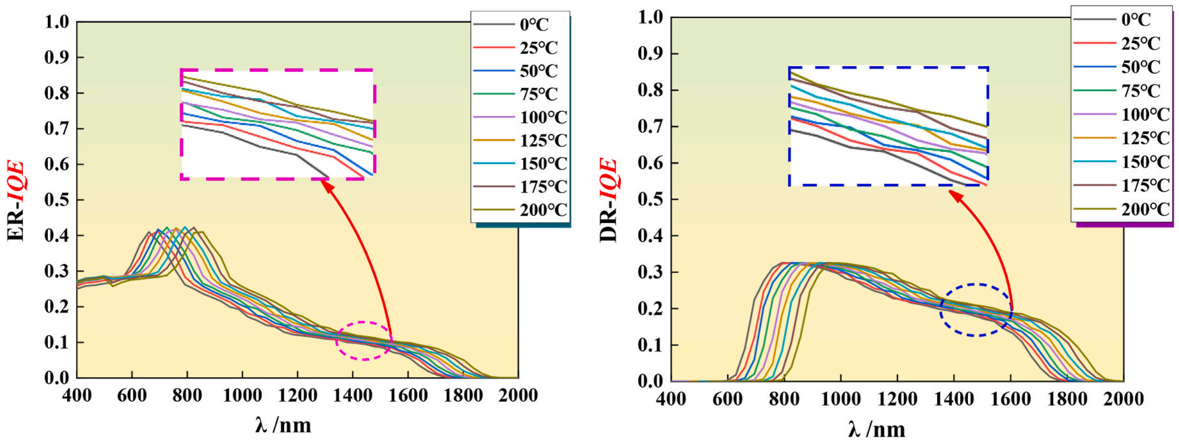

(a) Emission Region (ER)

(b) Depletion Region (DR)

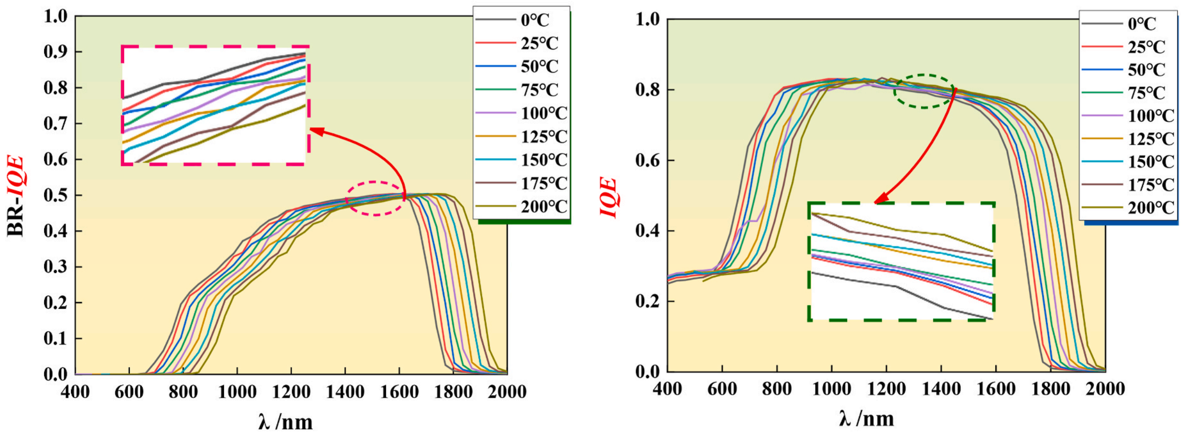

(c) Base region (BR)

(d) Internal quantum efficiency (*IQE*)

**Fig. 8.** The relationship between ER, DR, BR, *IQE*, and temperature.

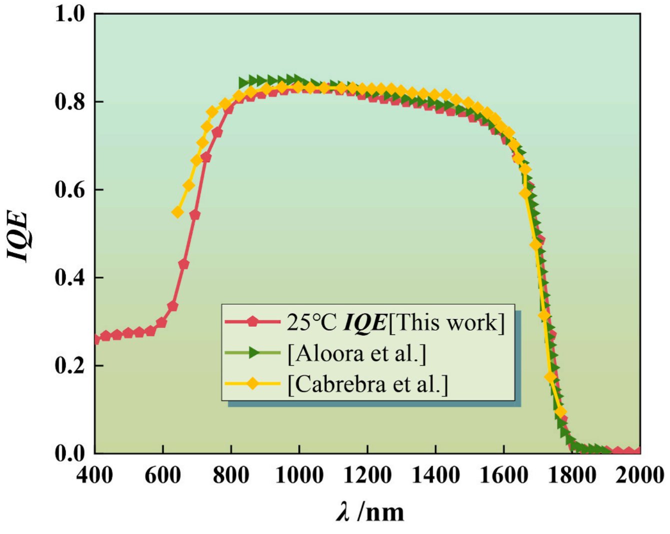

**Fig. 9.** Comparison between model and experimental data.

the internal quantum efficiency also increases with rising temperatures. In the DR, the peak value of DR conversion efficiency is about 33 %. When the temperature ranges from 0 to 200 °C, the peak of conversion efficiency is mainly concentrated in the range of 780–980 μm. Similar to the trend observed in the ER, the overall curve experiences a redshift as the temperature increases. Before reaching the peak value, the DR-*IQE* decreases with the increase in temperature. After the peak value, the DR-*IQE* increases with the increase in temperature. In the BR, the peak value of ECE occurs after 1.6 μm, and the peak value of ECE is about 50 %. Fig. 8 (d) shows the *IQE* obtained by the sum of three regions. It shows that the increase in temperature will change the *IQE* of the TPV cell, thus affecting the ECE.

In Fig. 9, the results of *IQE* obtained using the calculation model in this paper are compared with the results in the literature [45,62]. Through comparison, it can be found that the results are consistent in the wavelength range of 1000–1900 nm. In the range of 800–1000 nm, there is a maximum difference of about 4.45 %. The main reason for this discrepancy is that the initial doping concentration in ER is slightly different from that in the literature. Specifically, the initial doping concentration in the ER in literature [62] is nearly 10 times higher than that in this paper. This variation is within the allowable range, supporting the reliability of our model calculations.

Fig. 10 shows the variation of the maximum current ($I_m$), maximum voltage ($V_m$), short circuit current ($I_{sc}$), and open circuit voltage ($V_{oc}$) of

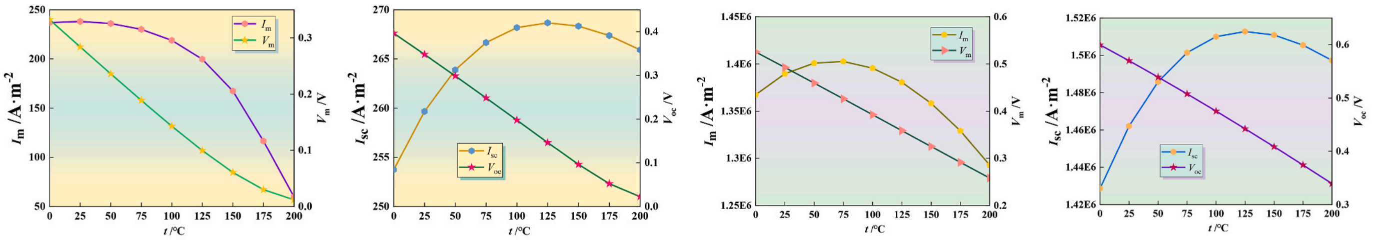

(a1) $T_e$= 1000 K (a2) $T_e$= 1000 K (d1) $T_e$=2500 K (d2) $T_e$=2500 K

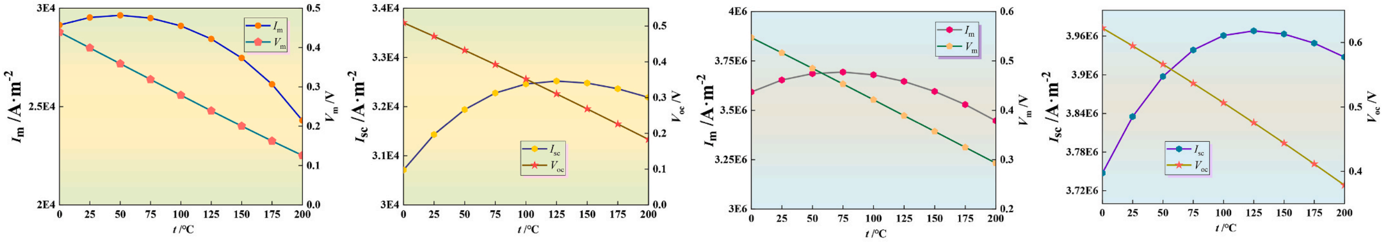

(b1) $T_e$= 1500 K (b2) $T_e$= 1500 K (e1) $T_e$=3000 K (e2) $T_e$=3000 K

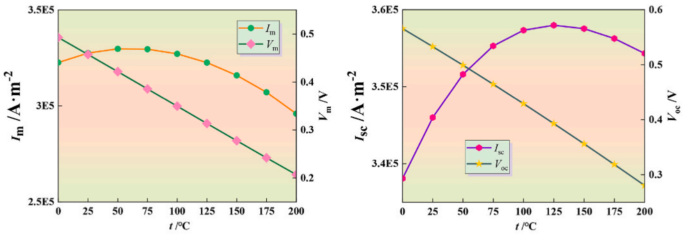

(c1) $T_e$= 2000 K (c2) $T_e$= 2000 K

**Fig. 10.** Variation of cell electrical performance parameters with temperature under different heat source temperatures.

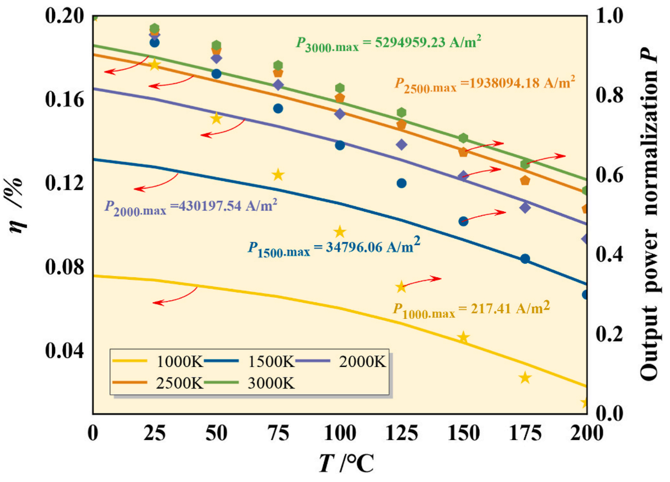

**Fig. 11.** Energy conversion efficiency of TPV cell.

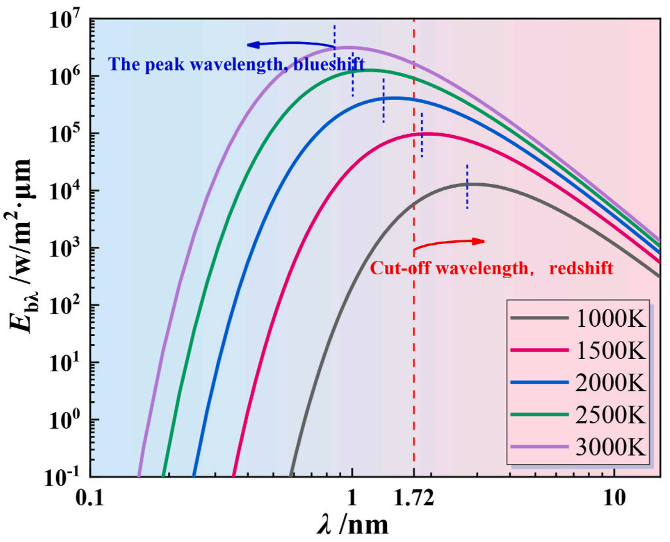

**Fig. 12.** The spectral emissive power of blackbody at several temperatures.

the TPV cell at different cell temperatures (0–200 °C) with emitter temperatures set at 1500 K, 2000 K, 2500 K, and 3000 K. From the overall trend in the figure, the $I_m$, $V_m$, $I_{sc}$, and $V_{oc}$ of the cell all increase but their trends are different as the temperature of the radiation source increase. As the cell temperature increases, the curve trend of $I_m$ increases first and then decreases. When the temperature of the radiator is 1000 K, the peak value of $I_m$ is 25 °C. At the temperature of the emitter of 1500 K, the peak value of the $I_m$ is 50 °C. The temperature of the radiator is 2000–3000 K, and the peak value of $I_m$ is 75 °C. The $V_m$ is negatively related to the cell temperature. The $V_m$ drops by about 0.3 V for every 25 °C rise in the cell temperature, which is not affected by the temperature of the radiator. The $I_{sc}$ generally increases with the rising cell temperature. But with the increase of cell temperature, the $I_{sc}$ increases at a slower rate. The $V_{oc}$ decreases with increasing cell temperature, exhibiting a negative correlation. In general, the larger the bandgap energy, the higher the open circuit voltage. The smaller the band gap

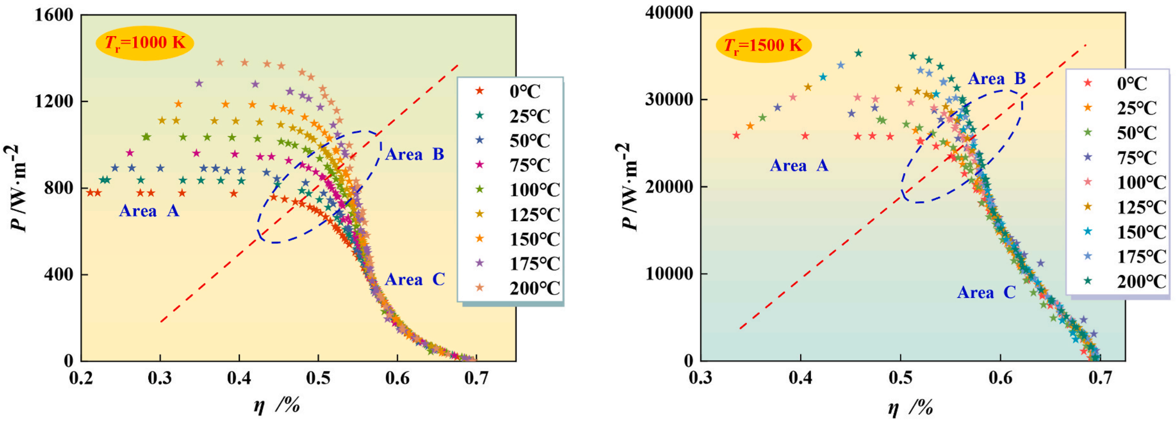

(a) $T_e = 1000$ K

(b) $T_e = 1500$ K

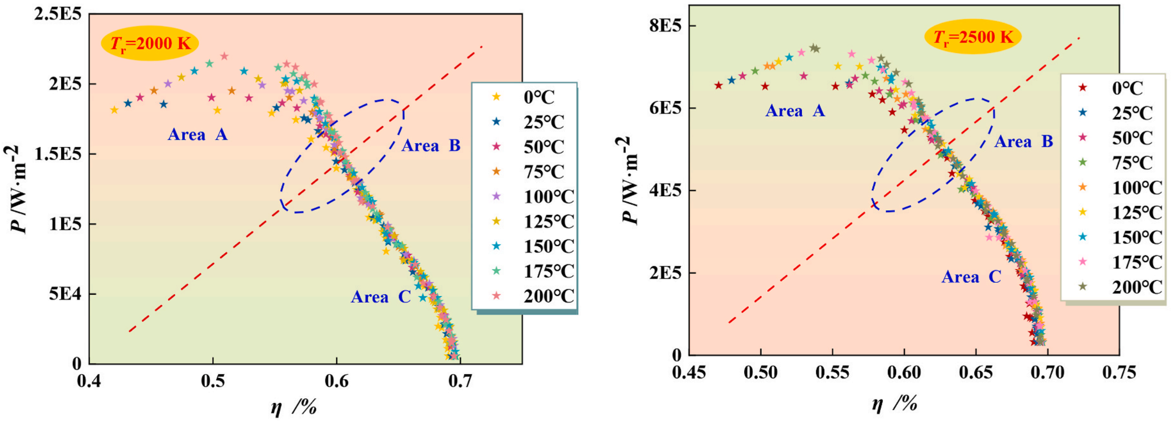

(c) $T_e = 2000$ K

(d) $T_e = 2500$ K

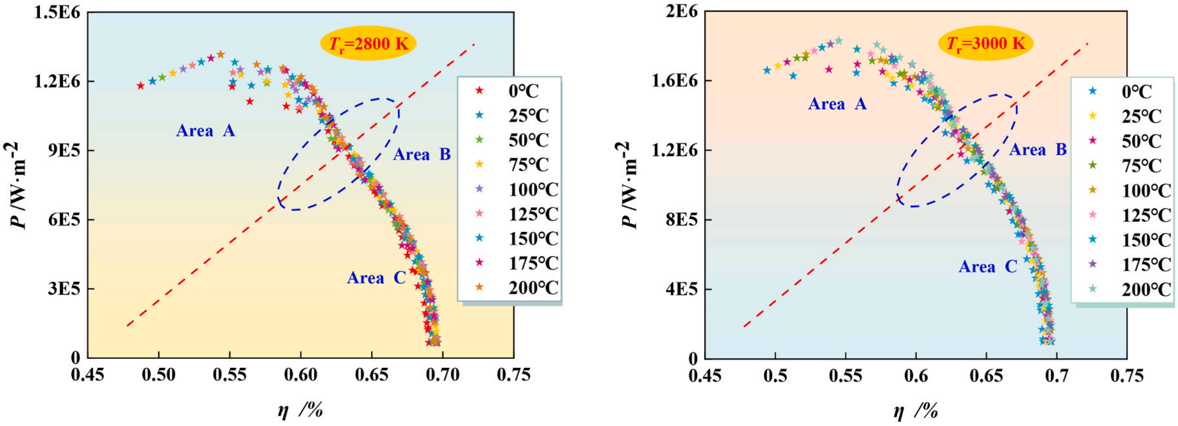

(e) $T_e = 2800$ K

(f) $T_e = 3000$ K

**Fig. 13.** Pareto optimal solution for efficiency and output power.

energy, the higher the short-circuit current. The cause of this phenomenon can be explained by the Fermi energy level of semiconductor material. When the injected photon energy is fixed, the increase in temperature will cause more electrons to be distributed in the defect state with a higher energy state, resulting in an increase in the Fermi energy level, which will affect the distribution of the carrier. In general, with the increase in temperature, the probability of the electron occupying energy less than the Fermi level quantum state decreases, while the probability of occupying energy higher than the Fermi level quantum state increases.

Fig. 11 shows the curve of the ECE of the cell changing with the cell temperature under the different temperatures of the radiator. The ECE of the cell declines as cell temperature rises. When the temperature of $T_c$ is fixed, the higher the temperature of the emitter, the higher the ECE of the cell. However, even if the selected spectral range is 0.4–2.0 μm, the ECE of the cell is low. When the temperature of the emitter is up to 3000 K, the ECE is still less than 20 %. On the one hand, as the temperature of the emitter increases, the peak wavelength shifts towards the shortwave

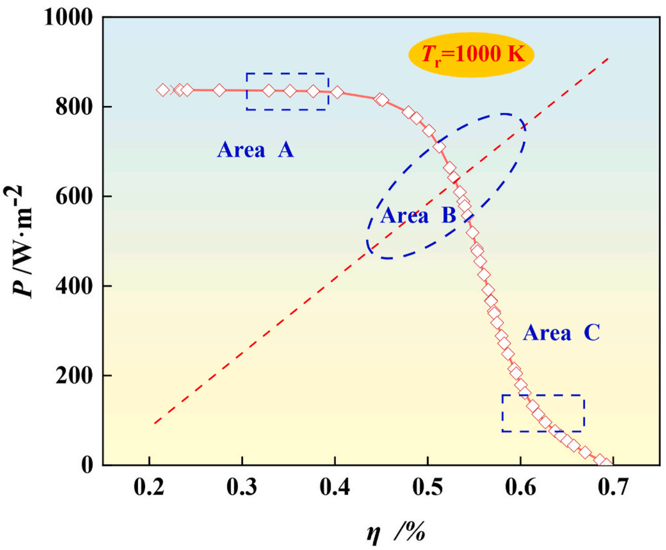

**Fig. 14.** The detailed diagram of the output power and efficiency curve.

**Table 1**
The best spectral range and conversion efficiency of GaSb at different temperatures of the radiator.

| Area | Spectral range (μm) | Bandwidth (μm) | $\eta$ (%) | $P$ (W·m$^{-2}$) |
|---|---|---|---|---|
| A | 0.4583-1.8469 | 1.3886 | 32.88 | 835.71 |
| | 0.5284-1.8234 | 1.2950 | 35.15 | 835.22 |
| | 0.5068-1.7998 | 1.2930 | 37.66 | 834.45 |
| B | 0.6129-1.6064 | 0.9935 | 53.47 | 609.10 |
| | 0.6428-1.5801 | 0.9373 | 54.33 | 556.72 |
| | 0.6526-1.5392 | 0.8866 | 55.37 | 477.46 |
| C | 0.6668-1.3144 | 0.6476 | 60.48 | 160.93 |
| | 0.8087-1.2588 | 0.4501 | 61.94 | 113.50 |
| | 0.6423-1.1993 | 0.5570 | 63.73 | 76.027 |

direction. On the other hand, it is influenced by the manufacturing process of the cell itself. Meanwhile, it is difficult to reach such a high temperature. Moreover, the emissivity of the emitter in the effective band is far less than 1, and the energy conversion performance of the cell will be lower. We should better adjust the available spectral range according to the temperature of the cell and emitter.

### *3.4. Maximization of TPV performance*

Fig. 12 displays the spectral emissive power of the emitter that maximizes conversion efficiency while taking the cell temperature into account. With the increase in temperature of the TPV cell, the band gap energy decreases, as shown in Fig. 6(a). According to Eq. (10), it can be inferred that as the bandgap energy decreases, the cut-off wavelength increases (redshifts) of the cell. However, the peak wavelength appears blueshift as the temperature of the heat source increases. This will change the output power density and the proportion of heat loss of the cell. Therefore, it is necessary to determine the optimal spectral matching range at different temperatures of the cell through the TPV -GA model to maximize the output power of the cell.

Calculate the emitter emission spectrum that maximizes TPV conversion efficiency at a given cell temperature. This spectral range was obtained from the TPV-NSGA-II model, using 120 small spectral bands, each with a bandwidth of 0.05 μm, within the energy range of 0.041 eV, to minimize computation time. Note that the differences in conversion efficiency, the output power density, and the width and spectral cutoffs of the ideal emission spectrum are all less than 1 % when the spectral discretization is refined from 100 to 200 bands.

Fig. 13 shows the optimal solutions for efficiency and power density output of the cell at various temperatures with different emitter temperatures. From the figure, it can be seen the data distribution is clearly divided into three regions, referred to as Zone A, Zone B, and Zone C. These regions are roughly divided based on the curve y = x as the central line. However, the characteristics of the three regions are apparent. The output energy flow density and ECE are both high in Zone A. On the contrary, Zone C exhibits high thermoelectric conversion efficiency but low output power density. Zone B is characterized by relatively high efficiency and output power density. We have identified corresponding regions for practical applications based on different application requirements. To provide further interval analysis, we have plotted Fig. 14.

Fig. 14 illustrates the detailed output power and efficiency curves depicted in Fig. 13 (a) for a heat source temperature of 1000 K and a cell temperature of 25 °C. Three points from three regions were selected, and their corresponding intervals, efficiency, and power density values are summarized in Table 1. Based on the data in Tables 1 and it can be seen region A has an extensive spectral range and input energy, resulting in a high output power density. Additionally, the curve changes in region A are relatively gentle, indicating that the overall effective spectral range of region A is wider and has more incident energy. Region C has a narrow spectral range and less input energy, resulting in a low output power density. Moreover, the effective spectral range in region C is narrow, and the internal quantum efficiency is high, resulting in a high thermoelectric conversion efficiency. Region B belongs to the compromised region, with high efficiency and power density. Whether selecting the highest efficiency or maximum spectrum, it corresponds to the corresponding spectral bandwidth.

## 4. Conclusions

To maximize the utilization of TPV cells and rationalize efficiency and power density in different working environments, a framework is proposed that combines a multi-objective genetic algorithm (NSGA-II) with the internal quantum efficiency (*IQE*) of the TPV cell, which accounts for both thermal and electric factors. The spectrally selective emitter used in the condition for the TPV system under consideration has a temperature range of 1000–3000 K, a spectral range of 0.4–2.0 μm, and the cell temperature changes range from 0 to 200 °C. The result can be summarized as follows.

(1) The effect of temperature on ER, DR, and BR zones is different. In the ER, the peak value of conversion efficiency moves toward the direction of the long wave (redshift) as the cell temperature rises. Following the peak value, as the wavelength increases, the internal quantum efficiency conversion also increases with temperature. In the DR, When the temperature is 0–200 °C, the peak of conversion efficiency is mainly concentrated in the range of 780–980 μm. Similar to the ER, the overall trend also moves toward the direction of the long wave with the rise of temperature. The internal quantum efficiency is influenced by the temperature of the cell.

(2) When $T_e$ is fixed, the rise in temperature of the cell will reduce the ECE of the cell. If the temperature of $T_c$ is fixed, the higher the temperature of the emitter, the higher the ECE of the cell. Even if the selected spectral range is 0.4–2.0 μm, the temperature of the emitter is up to 3000 K, and the ECE is still less than 20 %.

(3) By combining the internal quantum efficiency (*IQE*) of TPV cells considering thermal loss with the NSGA-II, the optimal match between the cell and the spectral control emitter is explored, and the data distribution is divided into three regions. Based on different requirements for efficiency and output power, corresponding regions in practical applications can be selected according to different application requirements.

From a practical standpoint, the production and processing of TPV cells are complex and challenging. Exploring new production techniques and developing new materials requires time and practice. Moreover, the introduction of new processes and materials may lead to increased costs, making rapid application and promotion more challenging. Therefore, it is essential to maximize the performance advantages of existing products. Based on the optimization framework proposed in this article, it is feasible to maximize energy conversion. After clarifying the temperature of the heat source and the cell, a spectrum selection emitter can be employed through our proposed framework to achieve maximum efficiency or maximum output power density within the allowed spectral range of different TPV cells. Although this framework has limitations when applied to real-world TPV systems, such as in our hypothesis that the spectral range of the emitter is set at 0.4–2.0 μm with an emissivity of 1. This is difficult to achieve in the manufacturing of selective emitter. Furthermore, maintaining the cell at a stable low temperature at all time is also difficult. If higher-performing emitters can be produced through reasonable spectral regulation and reduced thermal pressure, our proposed framework can be more effectively applied in practice. Ultimately, it will be possible to maximize the benefits of the TPV system and foster its further development.

## CRediT authorship contribution statement

**Xiu-Li Liu:** Writing – original draft, Investigation, Formal analysis, Data curation. **Xiao-Lei Li:** Software. **Xin-Lin Xia:** Writing – review & editing, Funding acquisition. **Xue Chen:** Funding acquisition.

## Declaration of competing interest

The authors declare that they have no known competing financial interests or personal relationships that could have appeared to influence the work reported in this paper.

## Acknowledgements

This work is supported by the Heilongjiang Touyan Innovation Team Program (No. XNAUEA5640206420), the National Natural Science Foundation of China (No. 52406080) and the National Natural Science Foundation of China (No. 52276058).

## Appendix A. Supplementary data

Supplementary data to this article can be found online at https://doi.org/10.1016/j.renene.2024.121544.

## References

[1] B. Wernsman, et al., Greater than 20% radiant heat conversion efficiency of a thermophotovoltaic radiator/module system using reflective spectral control, IEEE Trans. Electron. Dev. 51 (3) (2004) 512–515.

[2] R.D. Koudelka, Radioisotope micropower system using thermophotovoltaic energy conversion, AIP Conf. Proc. (2006) 545–551.

[3] F. Wang, et al., Effects of non-uniform porosity on thermochemical performance of solar driven methane reforming, Energy 191 (2020).

[4] Q. Peng, et al., Experimental investigation on premixed hydrogen/air combustion in varied size combustors inserted with porous medium for thermophotovoltaic system applications, Energy Convers. Manag. 200 (2019) 112086.

[5] B. Xie, et al., Effect of pins and exit-step on thermal performance and energy efficiency of hydrogen-fueled combustion for micro-thermophotovoltaic, Energy 239 (2022) 122341.

[6] A. Datas, Optimum semiconductor bandgaps in single junction and multijunction thermophotovoltaic converters, Sol. Energy Mater. Sol. Cell. 134 (2015) 275–290.

[7] G. Colangelo, et al., New approaches to the design of the combustion system for thermophotovoltaic applications, Semicond. Sci. Technol. 18 (5) (2003) S262–S269.

[8] A. Datas, et al., Ultra high temperature latent heat energy storage and thermophotovoltaic energy conversion, Energy 107 (2016) 542–549.

[9] Z. Utlu, B.S. Önal, Thermodynamic analysis of thermophotovoltaic systems used in waste heat recovery systems: an application, Int. J. Low Carbon Technol. 13 (1) (2018) 52–60.

[10] D. Erik, et al., Combined solar power and TPV, World Renewable Energy Congress 6 (2011) 8–13.

[11] W.R. Chan, et al., Toward high-energy-density, high-efficiency, and moderate-temperature chip-scale thermophotovoltaics, Proc Natl Acad Sci U S A 110 (14) (2013) 5309–5314.

[12] K. Qiu, A.C.S. Hayden, Direct thermal to electrical energy conversion using very low bandgap TPV cells in a gas-fired furnace system, Energy Convers. Manag. 79 (2014) 54–58.

[13] D. Li, Y. Xuan, Design and evaluation of a hybrid solar thermphotovoltaic-thermoelectric system, Sol. Energy 231 (2022) 1025–1036.

[14] E. López, et al., Thermophotovoltaic conversion efficiency measurement at high view factors, Sol. Energy Mater. Sol. Cell. 250 (2023) 112069.

[15] C. Meng, et al., Selective emitter with core–shell nanosphere structure for thermophotovoltaic systems, Energy 239 (2022) 121884.

[16] Z. Omair, et al., Ultraefficient thermophotovoltaic power conversion by band-edge spectral filtering, Proc Natl Acad Sci U S A 116 (31) (2019) 15356–15361.

[17] M.M.A. Gamel, et al., Multi-dimensional optimization of In(0.53)Ga(0.47)As thermophotovoltaic cell using real coded genetic algorithm, Sci. Rep. 11 (1) (2021) 7741.

[18] M.P. Bernardi, et al., Impacts of propagating, frustrated and surface modes on radiative, electrical and thermal losses in nanoscale-gap thermophotovoltaic power generators, Sci. Rep. 5 (2015) 11626.

[19] M. Francoeur, et al., Thermal impacts on the performance of nanoscale-gap thermophotovoltaic power generators, IEEE Trans. Energy Convers. 26 (2) (2011) 686–698.

[20] A. LaPotin, et al., Thermophotovoltaic efficiency of 40, Nature 604 (7905) (2022) 287–291.

[21] J.A.P.E. Skoplaki, On the temperature dependence of photovoltaic module electrical performance: a review of efficiency/power correlations, Sol. Energy 83 (2009) 614–624.

[22] N.M.R. Priyanka Singh, Temperature-dependence-of-solar-cell-perfor_2012_Solar-Energy-Materials-and, Sol. Energy Mater. Sol. Cells 101 (2012) 36–45.

[23] E. Vadiee, et al., Temperature dependence of GaSb and AlGaSb solar cells, Curr. Appl. Phys. 18 (6) (2018) 752–761.

[24] P. Talebizadeh, et al., Prediction of the optimum slope and surface azimuth angles using the Genetic Algorithm, Energy Build. 43 (11) (2011) 2998–3005.

[25] M.M. Keshtkar, P. Talebizadeh, Multi-objective optimization of cooling water package based on 3E analysis: a case study, Energy 134 (2017) 840–849.

[26] M. Ghalambaz, et al., Building energy optimization using Grey Wolf optimizer (GWO), Case Stud. Therm. Eng. 27 (2021).

[27] M. Ghalambaz, et al., Building energy optimization using butterfly optimization algorithm, Therm. Sci. 26 (5 Part A) (2022) 3975–3986.

[28] Y. Fan, et al., Random reselection particle swarm optimization for optimal design of solar photovoltaic modules, Energy 239 (2022).

[29] H. Han, et al., Multi-objective optimization of corrugated tube with loose-fit twisted tape using RSM and NSGA-II, Int. J. Heat Mass Tran. 131 (2019) 781–794.

[30] Q. Cai, et al., Performance analysis of GaSb cell and thermophotovoltaic system under near-field thermal radiation, Int. J. Thermophys. 41 (12) (2020).

[31] R. Abbassi, et al., Identification of unknown parameters of solar cell models: a comprehensive overview of available approaches, Renew. Sustain. Energy Rev. 90 (2018) 453–474.

[32] C. Zhang, et al., A novel thermophotovoltaic optical cavity for improved irradiance uniformity and system performance, Energy 195 (2020).

[33] A.M.A. Soliman, H. Hassan, 3D study on the performance of cooling technique composed of heat spreader and microchannels for cooling the solar cells, Energy Convers. Manag. 170 (2018) 1–18.

[34] G. Stollwerck, et al., Characterization_and_simulation_of GaSb device-related properties, IEEE Trans. Electron. Dev. 47 (2000) 448–457.

[35] E.B. Elkenany, Theoretical investigations of electronic, optical and mechanical properties for GaSb and AlSb semiconductors under the influence of temperature, Spectrochim. Acta Mol. Biomol. Spectrosc. 150 (2015) 15–20.

[36] L. Tang, et al., N-type vapor diffusion for the fabrication of GaSb thermophotovoltaic cells to increase the quantum efficiency in the long wavelength range, Sol. Energy Mater. Sol. Cell. 194 (2019) 137–141.

[37] W. Xu, et al., Simulation of Zinc-diffused InAs cells for low temperature thermophotovoltaic systems, Infrared Phys. Technol. 115 (2021) 103719.

[38] B. Roy-Layinde, et al., Sustaining efficiency at elevated power densities in InGaAs airbridge thermophotovoltaic cells, Sol. Energy Mater. Sol. Cell. 236 (2022) 111523.

[39] G. Stollwerck, et al., Characterization and simulation of GaSb device-related_ properties, IEEE Trans. Electron. Dev. 47 (2000) 448–457.

[40] Y.P. Varshni, Temperature dependence of the energy gap in semiconductors, Physica 34 (1) (1967) 149–154.

[41] L.M. Fraas, et al., Fundamental characterization studies of GaSb solar cells. The Conference Record of the Twenty-Second IEEE Photovoltaic Specialists Conference - 1991, 1991, pp. 80–84.

[42] M. Sotoodeh, et al., Empirical low-field mobility model for III–V compounds applicable in device simulation codes, J. Appl. Phys. 87 (6) (2000) 2890–2900.

[43] X. Peng, et al., Broadband omnidirectional infrared nanophotonic spectral controller for GaInAsSb thermophotovoltaic cell, Sol. Energy Mater. Sol. Cell. 248 (2022) 111986.

[44] H. Ye, et al., The simulation and optimization of the internal quantum efficiency of GaSb thermophotovoltaic cells with a box-shaped Zn diffusion profile, Sol. Energy Mater. Sol. Cell. 125 (2014) 268–275.

[45] C. Algora, Modelling and manufacturing GaSb TPV converters, AIP Conf. Proc. (2003) 452–461.

[46] D. Martín, C. Algora, Temperature-dependent GaSb material parameters for reliable thermophotovoltaic cell modelling, Semicond. Sci. Technol. 19 (8) (2004) 1040–1052.

[47] D.L. Bouzid F, Performance evaluation of a GaSb thermophotovoltaic converter, Journal of Renewable Energies 15 (3) (2012) 383–397.

[48] Y. Wang, et al., Evaluation of thermal radiation dependent performance of GaSb thermophotovoltaic cell based on an analytical absorption coefficient model, Sol. Energy Mater. Sol. Cell. 94 (10) (2010) 1704–1710.

[49] L. Tang, et al., Suppression of the surface "dead region" for fabrication of GaInAsSb thermophotovoltaic cells, Sol. Energy Mater. Sol. Cell. 163 (2017) 263–269.

[50] D. Montesdeoca, et al., Open circuit voltage increase of GaSb/GaAs quantum ring solar cells under high hydrostatic pressure, Sol. Energy Mater. Sol. Cell. 187 (2018) 227–232.

[51] J.C.C. Fan, Theoretical temperature-dependence of solar-cell parameters, Sol. Cell. 17 (2–3) (1986) 309–315.

[52] W.E. Rashid, et al., Optimization of p-type emitter thickness for GaSb-based thermophotovoltaic cells. 13th IEEE International Conference on Semiconductor Electronics (IEEE ICSE), 2018, pp. 109–112. Kuala Lumpur, MALAYSIA.

[53] G. Wang, et al., The error analysis of the reverse saturation current of the diode in the modeling of photovoltaic modules, Energy 115 (2016) 478–485.

[54] X.-L. Liu, et al., A single spectral optical path design of the thermophotovoltaic system for improving irradiance intensity and uniformity, Energy Technol. 10 (9) (2022) 2200326.

[55] J. Tian, et al., Performance analysis and selective emitter design for an efficient concentrated solar thermophotovoltaic system based on cavity-structured absorber and high-bandgap cell, Therm. Sci. Eng. Prog. 40 (2023) 101767.

[56] L. Zhu, et al., Water immersion cooling of PV cells in a high concentration system, Sol. Energy Mater. Sol. Cell. 95 (2) (2011) 538–545.

[57] A. Royne, C.J. Dey, Design of a jet impingement cooling device for densely packed PV cells under high concentration, Sol. Energy 81 (8) (2007) 1014–1024.

[58] A. Reeser, et al., High quality flow boiling heat transfer and pressure drop in microgap pin fin arrays, Int. J. Heat Mass Tran. 78 (2014) 974–985.

[59] A. Reeser, et al., Energy efficient two-phase microcooler design for a concentrated photovoltaic triple junction cell, J. Sol. Energy Eng. 136 (3) (2014).

[60] J.E.A.L.M. Fraas, P.E. Gruenbaum, V.S. Sundaram, Fundamental characterization studies of GaSb solar cells. The 22nd IEEE Photovoltaic Specialist Conference (PVSC), 1991, pp. 80–84.

[61] C. Ghezzi, et al., Optical absorption near the fundamental absorption edge in GaSb, Phys. Rev. B 52 (3) (1995) 1463–1466.

[62] A. Cabrera, et al., Thermophotovoltaic efficiency measurement: design and analysis of a novel experimental method. 12th Spanish Conference on Electron Devices (CDE), 2018. Salamanca, SPAIN.